

# Stability Characteristics of the Mesopause Region above the Andes

Fan Yang<sup>1</sup> and Alan Z Liu<sup>1</sup>

<sup>1</sup>Embry-Riddle Aeronautical University

November 22, 2022

## Abstract

We report a detailed analysis of characteristics of stability based on high-resolution temperature and horizontal wind measurement made with a Na lidar at the Andes Lidar Observatory, located in Cerro Pachón, Chile (30.2° S, 70.7° W). The general probability of convective and dynamical instability are 5.3% and 16.4%. Contributions from different scales of GWs have been calculated. Large wind shear and dynamical instabilities are mainly generated because all GWs with different frequencies exist simultaneously. Isolated parts of GWs have much less contribution to the generation of instabilities. The dynamical instability is mainly contributed from less stable stratification and large wind shear together. Either factor can lead to about 15% of dynamical instability. Biases of the instability probabilities due to photon noise have been analyzed, and the biases have been subtracted from the measured probabilities.



## Abstract

We report a detailed analysis of characteristics of stability based on high-resolution temperature and horizontal wind measurement made with a Na lidar at the Andes Lidar Observatory, located in Cerro Pachón, Chile (30.2° S, 70.7° W). The general probability of convective and dynamical instability are 5.3% and 16.4%. Contributions from different scales of GWs have been calculated. Large wind shear and dynamical instabilities are mainly generated because all GWs with different frequencies exist simultaneously. Isolated parts of GWs have much less contribution to the generation of instabilities. The dynamical instability is mainly contributed from less stable stratification and large wind shear together. Either factor can lead to about 15% of dynamical instability. Biases of the instability probabilities due to photon noise have been analyzed, and the biases have been subtracted from the measured probabilities.

## 1 Introduction

It is widely known that gravity waves (GWs) transport their energy and momentum from the lower atmosphere to the mesosphere and lower thermosphere (MLT). As these waves reach large amplitudes, they dissipate and deposit energy and momentum in this region, impart significant forcing to the global atmospheric circulation. GWs are dissipated primarily through instabilities processes: convective instability (CI) that occurs when large-amplitude waves create a negative vertical potential temperature gradient [Hodges, 1967], and dynamic (shear) instability (DI) when a large vertical gradient of horizontal wind is created by wave motion or momentum deposition [Fritts and Rastogi, 1985]. Other instability processes could happen under specific conditions, such as vortical-pair instability [Dong and Yeh, 1988], parametric instability [Klostermeyer, 1991], slantwise dynamical instability [Hines, 1971], and resonant instability [Phillips, 1977].

There are many works investigating the causes and characteristics of instabilities in the MLT region. Theoretical analysis suggested that inertia GWs might lead to KHI [Fritts and Yuan, 1989; Andreassen *et al.*, 1994, 1998]. Two-dimensional instabilities are closely related to second-order wave-wave interactions [Lombard and Riley, 1996]. Sonmor and Klaassen [1997] found the generation of different types of instabilities are related to the internal GWs with variable frequencies using a Floquet analysis of a monochromatic wave propagating in a uniformly stratified background. Liu *et al.* [1999] suggests that the in-

duced acceleration due to CI may lead to strong shear, which causes DI at lower altitudes. *Gardner et al.* [2002] suggested that instability can be generated when the combined perturbations associated with tides and GWs induce large vertical gradients in the horizontal wind and temperature profiles. *Li et al.* [2005a] found that wave-mean flow interactions contributed significantly to the generation of the strong ( $>40$  m/s/km) wind shear and dynamically unstable layers (DUL). *Yue et al.* [2010] found that about 60% of the large wind shear formation is driven by long-period waves such as tidal-period perturbations. 2D model result showed that the momentum deposited by breaking GWs accelerates the mean wind creating a background condition that favors the occurrence of GWs instability [*Liu et al.*, 2014]. In the work of *Andrioli et al.* [2017], they suggested that GWs with period larger than 30 minutes should be responsible for keeping the long duration of DUL.

While theoretical and modeling studies have provided much insights into what types of instabilities could happen in different conditions and how they develop, there is lack of observational evidence of the frequencies these instabilities actually happen. The occurrence frequencies of these instabilities directly affect the net effect of GW breaking. Due to the highly intermittent nature of GWs [*Cao and Liu*, 2016], the instabilities are expected to happen intermittently as well. Observationally, while it is now possible to directly observe GW breaking using high resolution imaging [*Hecht et al.*, 2021], it is impossible to detect all GW breaking events even at a single location, due to limitations of instrument operation time and resolutions.

To estimate of the occurrence frequencies of instabilities, we can use the atmospheric stability parameters as a proxy, namely the square of buoyancy frequency ( $N^2$ ) and the Richardson number ( $Ri$ ). Although stable and unstable conditions described by stability parameters do not always correspond to the absence and presence of instabilities [*Achatz*, 2007], these parameters are the best measure available to infer the likelihood of occurrence of instabilities.

The observational data needed to calculate  $N^2$  and  $Ri$  are high temporal and vertical resolution profiles of temperature and horizontal wind in the MLT, which are not widely available. The only technique that can currently make such measurements is using a narrow-band Doppler resonance-fluorescence lidar, which probe the naturally occurring metal layers in the 80–110 km altitude region using lasers that excite specific metal atoms and detect their fluorescence signals [*She et al.*, 2021, and references therein]. The lasers

74 must have narrow enough line width ( $<100$  MHz) to be able to probe both Doppler broad-  
75 ening and Doppler shift of the atomic spectral line to infer both temperature and wind.  
76 The most common metal probed is sodium (Na), due to its large cross section and high  
77 abundance in the mesopause region. The lidars also have to achieve high signal-to-noise  
78 ratio (SNR) to infer wind and temperature at sufficiently high resolutions to resolve GWs,  
79 typically on the order of  $\sim 1$  km in vertical and  $\sim 1$  min in time.

80 One of the first stability measurements based on lidar observations was made by  
81 a Na lidar at Starfire Optical Range (SOR), NM, which achieved high SNR by using a  
82 the 3.5 m astronomical telescope at the site. *Zhao et al.* [2003] used 32 nights (195 h) of  
83 its observations (at 90-sec and 500-m resolutions) to examine atmospheric stabilities at  
84 SOR ( $35^{\circ}\text{N}$ ,  $105^{\circ}\text{W}$ ), and found that the atmosphere is most likely to be unstable in win-  
85 ter and least likely in summer. *Li et al.* [2005b] analyzed 19 nights (133 h) of lidar data  
86 acquired by the same Na lidar operated at Maui, HI ( $20^{\circ}\text{N}$ ) with a 3.67-m telescope, at  
87 15-min and 500-m resolutions. They found that most of the convectively unstable (CU)  
88 and dynamically unstable (DU) layers are located above the mesosphere inversion layers  
89 with a tendency for the DU layers to develop below the CU layers. ? presented the verti-  
90 cal variations of the probabilities of large wind shears, DI and CI over Fort Collins, CO  
91 ( $41^{\circ}\text{N}$ ,  $105^{\circ}\text{W}$ ) based on the Na lidar measurement with a 35-cm telescopes and at res-  
92 olutions of 15 min and 2 km). They found the probability of CI is less than 1.4% for all  
93 seasons and the probability of DI ranges from 2.7% to 6.0%. More recently, *Andrioli et al.*  
94 [2017] studied the probabilities of the occurrence of CI and DI and their vertical distri-  
95 butions at São José dos Campos ( $23.1^{\circ}\text{S}$ ,  $45.9^{\circ}\text{W}$ ). They used a Na lidar that measured  
96 temperature only at 300-m and 3-min resolutions, and supplemented with wind measured  
97 by a meteor radar located at Cachoeira Paulista ( $22.7^{\circ}\text{S}$ ,  $45^{\circ}\text{W}$ ) at 1-hour and 2-km res-  
98 olutions. Based on 79 nights (589 h) of simultaneous data, they found CI presents much  
99 more seasonal variability than DI.

100 The purpose of this study is to present a stability analysis using a new set of high  
101 quality, extensive lidar data set obtained at the Andes Lidar Observatory in Cerro Pachón,  
102 Chile. The data used was acquired by a high-performance Na lidar on 244 nights over 5  
103 years with a total of 2170 hours. This high quality data set allows us to not only examine  
104 the overall stability properties but also investigate the effects of GWs with different peri-  
105 ods on the generation of unstable regions. The location of the site, in the Andes, is also a  
106 special region where many GWs are generated by the high Andes mountains so this anal-

107 ysis provides estimates of instability probabilities due to GWs from a different source than  
108 many previous studies.

109 The paper is organized as following. Section 2 describes the ALO lidar data of tem-  
110 perature and winds and the process applied to calculate the stability parameters. In sec-  
111 tion 3, we present the probability distributions of stability parameters. The contributions  
112 from GWs to the occurrence of instabilities are given in section 4. In section 5, the con-  
113 tributions to DI from stratification and wind shear are described. The results are further  
114 discussed in section 6. Conclusions are presented in section 7. Finally, in Appendix A,  
115 the numerical method for bias correction in calculating probabilities of instabilities is de-  
116 scribed in detail.

## 117 **2 Lidar Data and Calculation of Stability Parameters**

### 118 **2.1 Lidar Data**

119 The measurements of temperature and winds used for stability analysis are acquired  
120 with the Na lidar at Andes Lidar Observatory located at Cerro Pachón, Chile (30.3°S,  
121 70.7°W). The lidar's large power aperture product (0.66 Wm<sup>-2</sup>), reliable solid state laser,  
122 and efficient receiver optics [Liu *et al.*, 2016], combined with the high elevation site in  
123 the Andes with year around clear sky, make it feasible to acquire many nights of mea-  
124 surements at high temporal and spatial resolutions. In a normal operation mode, the laser  
125 beam was pointed toward zenith (Z), and 20° off zenith toward east (E) and south (S) in  
126 ZSZE sequence with typically 60-s time at each direction. This mode is used to measure  
127 temperature and all three wind components. On some nights, the laser beam was pointed  
128 to zenith only to make temperature and vertical wind measurements at higher temporal  
129 resolution. Horizontal winds measurements are not available for those nights. For this  
130 study, a total of 2170 hours of measurements from 244 nights, from May 2014 to Septem-  
131 ber 2019, are used. The total number of nights in each calendar month is summarized in  
132 Table.1, together with the numbers of nights when horizontal wind are available. An ex-  
133 ample of one night measurements of temperature and horizontal wind acquired on April  
134 18, 2015 are shown in Figure 1. It is clear that there were strong tidal motion and higher  
135 frequency fluctuations from GWs.

136 The lidar system obtained raw photon count data at 6-s temporal and 25-m range  
137 resolutions, which are then binned to 60-s temporal and 500-m vertical resolutions to de-

	Jan	Feb	Mar	Apr	May	Jun	Jul	Aug	Sep	Oct	Nov	Dec
nights	29	20	25	33	16	17	25	22	12	9	24	12
(with $U, V$ )	(4)	(6)	(14)	(25)	(11)	(17)	(25)	(11)	(5)	(8)	(24)	(10)

Table 1: Total numbers of nights of lidar measurements from May 2014 to September 2019 at ALO in each calendar month. These are the nights used to calculate  $N^2$ . The numbers in the parentheses are total nights when horizontal wind measurements were available. These are the nights used for wind shear and  $Ri$  calculations.

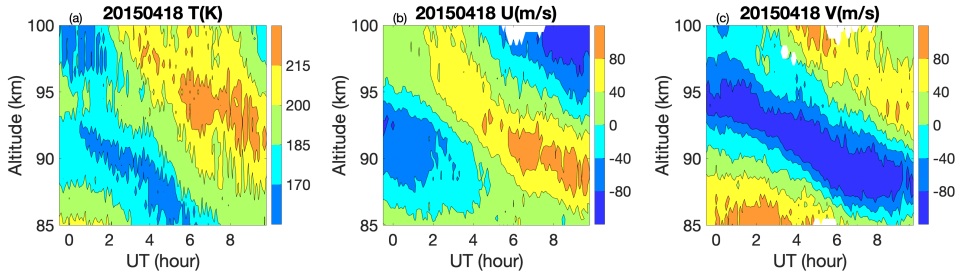


Figure 1: ALO Na Lidar measured  $T$ ,  $U$  and  $V$  on April 18, 2015.

138 rive the line-of-sight (LOS) temperature and winds. At these resolutions, the typical root  
 139 mean square (rms) errors for temperature and winds due to photon noise are respectively  
 140 no more than 2 K and 6 m/s in the 85 and 100 km altitude range. The error in horizon-  
 141 tal wind is simply the error in LOS wind divided by  $\sin 20^\circ$ . Errors grow fast beyond  
 142 this altitude range because of decreased Na density. We limit our analysis to the 85 to  
 143 100 km range and exclude measurements with large errors (horizontal wind error  $> 20$  m/s;  
 144 temperature error  $> 10$  K. 95% of data are retained with errors less than these 2 values.).  
 145 Temperatures and winds are further interpolated to uniform altitude and time intervals at  
 146 0.1 hour and 500 m to facilitate calculation of stability parameters. The smallest period  
 147 and vertical wavelength that can be resolved by the data are 12 min and 1 km, respectively.

## 148 2.2 Stability Parameters

149 The convective stability is measured by the square of buoyancy frequency  $N$  as

$$N^2 = \frac{g}{T} \left( \frac{\partial T}{\partial z} + \frac{g}{C_p} \right), \quad (1)$$

150 where  $g = 9.5 \text{ ms}^{-2}$  is the gravitational acceleration at the mesopause;  $T$  is atmospheric  
 151 temperature;  $z$  is altitude;  $C_p = 1004 \text{ Jkg}^{-1}\text{K}^{-1}$  is atmospheric specific heat at constant  
 152 pressure. When  $N^2$  is negative, the atmosphere is convectively unstable (CU) and has a  
 153 super-adiabatic lapse rate ( $-\partial T/\partial z > g/C_p$ ).

154 The dynamical stability is measured by the Richardson number  $Ri$  [Miles, 1961] as

$$Ri = \frac{N^2}{S^2}, \quad (2)$$

155 where

$$S = \left[ \left( \frac{du}{dz} \right)^2 + \left( \frac{dv}{dz} \right)^2 \right]^{1/2} \quad (3)$$

156 is the total vertical shear of horizontal wind and  $u$  and  $v$  are zonal and meridional wind  
 157 speeds, respectively.  $Ri < 0$  is equivalent to  $N^2 < 0$ , indicating convectively unstable  
 158 condition. When  $0 < Ri < 1/4$ , the atmosphere is considered as dynamically unstable.  
 159 Since a small positive  $Ri$  can be due to a very small positive  $N^2$  and/or large wind shear  
 160  $S$ , to further distinguish these two factors, we will also include  $S$  together with  $N^2$  and  $Ri$   
 161 as three stability parameters to analyze. Since for the nominal value of  $N^2 = 4 \times 10^{-4} \text{ s}^{-2}$ ,  
 162  $Ri < 1/4$  requires  $S > 40 \text{ ms}^{-1}\text{km}^{-1}$ , we use this value as the threshold to define large and  
 163 small wind shears.

164 The numerical calculation of these parameters involves vertical derivatives of  $T$ ,  
 165  $u$  and  $v$ , which are calculated using centered difference in vertical. For example,  $N^2$  at  
 166 height level  $k$  is calculated as

$$N_k^2 = \frac{g}{T_k} \left( \frac{T_{k+1} - T_{k-1}}{2\Delta z} + \frac{g}{C_p} \right), \quad (4)$$

167 where  $\Delta z = z_k - z_{k-1}$  is the vertical interval. The errors of calculated  $N^2$ ,  $S$ , and  $Ri$  come  
 168 from the errors in measured  $T$ ,  $u$  and  $v$ . The effect of these errors on the stability analysis  
 169 is discussed in more detail in the Appendix. The most important consequence of the mea-  
 170 surement error is they created a bias in the probability calculation. This bias is corrected  
 171 according to the method described in the Appendix.

172 An example of the three parameters derived from the same night of lidar measure-  
 173 ments in Figure 1 is shown in Figure 2. In the  $N^2$  plot, large blue areas indicate very  
 174 stable layers with large  $N^2$  values ( $N^2 > 7 \times 10^{-4} \text{ s}^{-2}$ ). The blue regions are moving  
 175 downward over the night, indicating influence of atmospheric tides. Red color indicates  
 176 convectively unstable regions where  $N^2 < 0$ . The convectively instability does not hap-

177 pen very often so the area of red region is small as expected. However, there is one such  
 178 region between 95 and 97 km that lasted over 2 hours before 2 UT.

179 The middle contour plot shows the wind shear  $S$ , where red regions represent large  
 180 wind shear ( $> 40 \text{ ms}^{-1}\text{km}^{-1}$ ). Just like the blue regions in the  $N^2$  plot, these large wind  
 181 shear regions were influence by the tides, and following closely with the region of high  
 182  $N^2$ . This is expected because only high  $N^2$  region can sustain high  $S$  to avoid it being de-  
 183 stroyed by dynamical instability. The similar features were found in lidar observations at  
 184 Maui [Li *et al.*, 2005b] and simulations with the Whole Atmosphere Community Climate  
 185 Model [Liu, 2017].

186 The right contour plot shows  $Ri$ , in which the red areas are by definition the same  
 187 as those in the  $N^2$  plot. The yellow areas are dynamically unstable where  $Ri$  is between  
 188 0 and 1/4. The yellow areas appeared intermittently, mainly in the regions of large wind  
 189 shear, and are overall more frequent than regions of negative  $N^2$ .

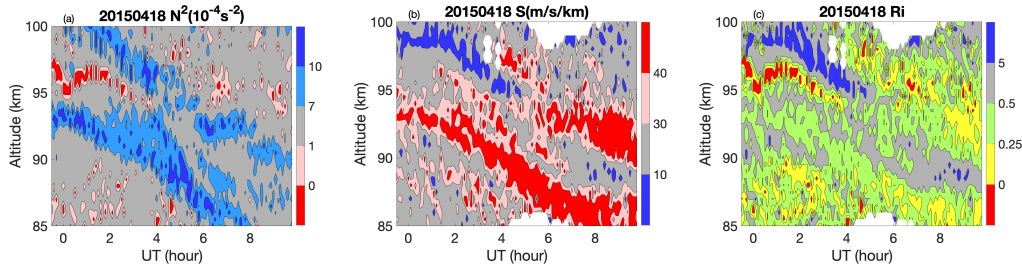


Figure 2: Time-altitude contours of  $N^2$ ,  $S$  and  $Ri$  on April 18, 2015 at ALO.

### 190 3 Distributions of Stability Parameters

191 For the purpose of this study, we define high-frequency (HF), medium frequency  
 192 (MF) and low-frequency (LF) GWs as with the observed periods less than 1 hour, between  
 193 1 to 6 hours, and longer than 6 hours, respectively. Our goal here is to isolate the effects  
 194 on stability properties due to GWs in each frequency range. Although such separation  
 195 does not take into account of the Doppler effect of the background wind on the intrinsic  
 196 periods, it is not expected to have much meaningful impact of the overall stability assess-  
 197 ment because (a) this Doppler effect changes the intrinsic periods both ways depending on  
 198 the relative direction of GW propagation and the background, and (b) the effect is not sig-

199 nificant for fast GWs. The details of separating waves in these three frequency ranges is  
 200 described in section 4.

201 The histograms of perturbations of  $T$ ,  $u$  and  $v$ , denoted as  $T'$ ,  $u'$  and  $v'$  respectively,  
 202 are shown in Figure 3. The three distributions in each plot corresponds to perturbations  
 203 in all frequencies, LF, and HF ranges (see Figure 3 caption for details). The distributions  
 204 that include all frequencies (black solid lines) follow closely a Gaussian distribution, in  
 205 agreement with previous lidar measurements [*Gardner and Yang, 1998*]. The LF GWs  
 206 have broader distribution than HF GWs, indicating that LF GWs have larger amplitudes.

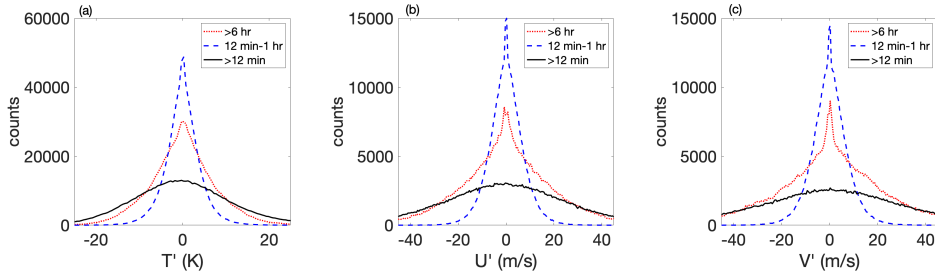


Figure 3: Histograms of  $T'$ ,  $u'$  and  $v'$ . The bin sizes are  $0.5 \text{ K}$ ,  $0.5 \text{ ms}^{-1}$  and  $0.5 \text{ ms}^{-1}$ , respectively. Black solid lines are perturbations at all time scales. Red dotted lines are perturbations with period  $> 6 \text{ hr}$  (LF GWs). Blue dashed lines are perturbations with period  $< 1 \text{ hr}$  (HF GWs).

207 The stability parameters  $N^2$ ,  $S$  and  $Ri$  are nonlinear functions of  $T$ ,  $u$  and  $v$  so their  
 208 distributions are non-Gaussian. Their distributions are illustrated with their histograms  
 209 shown in Figure 4. Here we focus on the distributions when all perturbations are included  
 210 (black solid lines). Since the variation of  $N^2$  is dominated by  $\partial T/\partial z$  in eq.(1), its distribu-  
 211 tion is close to Gaussian but with a long tail on the positive side. It peaks at  $3.2 \times 10^{-4} \text{ s}^{-2}$   
 212 with a median value of  $4.2 \times 10^{-4} \text{ s}^{-2}$ . The total wind shear  $S$  is a positive-definite quan-  
 213 tity and its histogram shown in Figure 4(b) is asymmetric with a long positive tail. It  
 214 peaks at  $16.8 \text{ ms}^{-1} \text{ km}^{-1}$  with a median value of  $20.8 \text{ ms}^{-1} \text{ km}^{-1}$ . The  $Ri$  distribution in  
 215 Figure 4(c) is highly asymmetric, with a long tail to the right and a much narrower range  
 216 to the left. It peaks at 0.32 with a median value of 0.8. In all three histograms, the shaded  
 217 area indicate negative  $N^2$ ,  $S > 40 \text{ ms}^{-1} \text{ km}^{-1}$ , and  $0 < Ri < 1/4$ , corresponding to convectively  
 218 unstable, large wind shear, and dynamically unstable regions, respectively, corresponding  
 219 to the red and yellow regions described earlier for Figure 1.

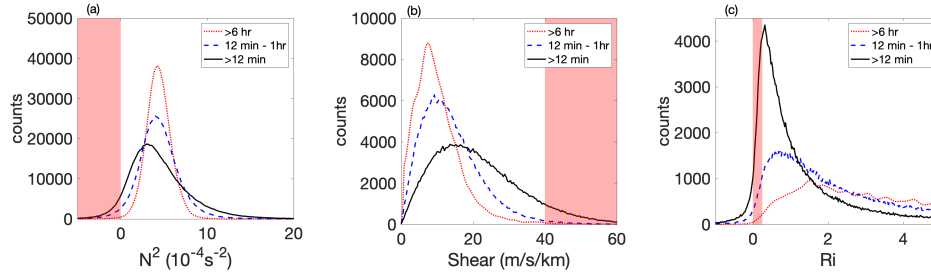


Figure 4: Histograms of  $N^2$ ,  $S$  and  $Ri$ . The bin sizes are  $0.2 \times 10^{-4} \text{ s}^{-2}$ ,  $0.4 \text{ ms}^{-1} \text{ km}^{-1}$  and  $0.02$ , respectively. Black solid lines are for stability parameters calculated from original lidar measurements which include waves with all periods ( $>12 \text{ min}$ ). Red dotted lines are calculated from data with periods  $>6 \text{ hr}$  (LF GWs). Blue dashed lines are calculated from data with periods  $<1 \text{ hr}$  (HF GWs). The shaded regions are  $N^2 < 0$ ,  $S > 40 \text{ ms}^{-1} \text{ km}^{-1}$ , and  $0 < Ri < 1/4$ , respectively.

220 The likelihood of occurrence of unstable regions or large wind shear is thus defined  
 221 as the fraction of the area under the distribution curve in the shaded area, which we refer  
 222 to as the Probability of Convective Instability (PCI), the Probability of Large Wind Shear  
 223 (PLW), and the Probability of Dynamical Instability (PDI), respectively. Note that due to  
 224 measurement errors, these distributions are wider than their true error-free distributions  
 225 because of the additional variances from the errors. Therefore, measurement errors intro-  
 226 duce a bias in the estimated probabilities. These biases however, can be corrected after  
 227 careful analysis of the relationship between error magnitudes and biases. This is described  
 228 in detail in the Appendix. As Figure 7 shows, the biases are significant for PLW and PDI  
 229 but small for PCI. They are positive for PCI and PLW and negative for PDI. Using all li-  
 230 dar measurements, we obtained bias-corrected  $\text{PCI}=4.0\%$ ,  $\text{PLW}=6.4\%$ , and  $\text{PDI}=15.9\%$ ,  
 231 with bias correction amounts of  $-0.02\%$ ,  $-2.5\%$ ,  $4.2\%$ , respectively. These values indicate  
 232 that overall, dynamically unstable and large wind shear regions are much more likely to  
 233 occur than convectively unstable regions, consistent with the observation in Figure 1.

234 The vertical distribution of probabilities are shown in Figure 5. The probabilities  
 235 are calculated with original data (including all waves) for each  $3 \text{ km}$  vertical bin at every  
 236  $0.5 \text{ km}$ . The PCI has a minimum around  $90 \text{ km}$  at about  $2.3\%$  and increases both above  
 237 and below this altitude to about  $6\text{-}7\%$ . The PLW decreases with altitude from  $85$  to  $97 \text{ km}$   
 238 then increases rapidly above. This is consistent with the rapid increase of wind speed  
 239 above  $100 \text{ km}$  measured by decades of rockets experiments [Larsen, 2002]. The PDI also

240 has a minimum about 14.8% at 90 km and increases to about 18.1% at 85.5 km and 18.6%  
 241 at 98.5 km.

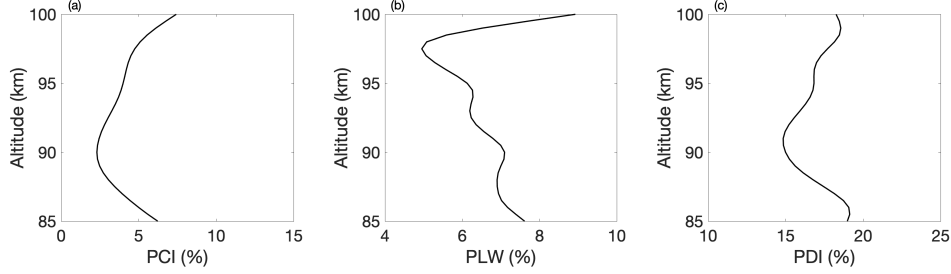


Figure 5: PCI, PLW, and PDI as functions of altitudes, calculated from original data (including all waves). The probabilities are calculated using all data within a 3-km altitude bin at each 500 m.

## 242 4 Gravity Wave Effects on Stability Parameters

### 243 4.1 Frequency dependence of GW contributions to PCI, PLW and PDI

244 It is expected that the mean background atmosphere in MLT is stable. Unstable lay-  
 245 ers occur temporarily and are mostly due to gravity waves (GWs) that generate large verti-  
 246 cal gradients of temperature and/or horizontal wind. As described in the previous section,  
 247 we define high-frequency (HF, <1 hr), medium frequency (MF, 1–6 hr) and low-frequency  
 248 (LF, >6 hr) and assess the effects on stability properties due to GWs in each period range.  
 249 The specific procedure of separating these GWs are described as following.

250 We first filter the original temperature and wind data (denoted as  $X$ ) with a low-  
 251 pass 1-hr and a 6-hr full-width Hamming window, and denote the filtered data as  $X_{1hr}$  and  
 252  $X_{6hr}$ , respectively. The nightly averaged wind and temperature are considered to be the  
 253 background (BG) and denoted as  $X_B$ . We can then calculate the follow quantities

$$\begin{aligned} X_{BH} &= X_B + X - X_{1hr}, & X_{BM} &= X_B + X_{1hr} - X_{6hr}, & X_{BL} &= X_{6hr}, \\ X_{BHM} &= X_B + X - X_{6hr}, & X_{BHL} &= X - X_{1hr} + X_{6hr}, & X_{BML} &= X_{1hr}. \end{aligned} \quad (5)$$

254 where the subscripts denote the components included: B for Background, H for HF GWs,  
 255 M for MF GWs, and L for LF GWs. For example,  $X_{BHM}$  includes the background, HF  
 256 and MF GWs but not LF GWs. With this notation, the distributions of stability parameters  
 257 shown in Figure 4 are for  $X$  (>12 min),  $X_{BH}$  (12 min to 1 hr), and  $X_{BL}$  (>6 hr).

We calculated the stability parameters for all combination of GWs in (5), and their distributions were obtained. For each distribution, PCI, PLW and PDI were calculated as illustrated in Figure 4. Their differences represent the changes in probabilities when certain types of GWs are added to a field. These probability changes for various scenarios are listed in Tables 2, 3, and 4. For example, in Table 2, the value in row HM and column B represents the change of PCI when HF and MF GWs are added onto the background flow (an increase of 2.7 percentage point). There are two clear patterns shown in these tables:

1. For PCI and PDI, HF GWs contribute most to their increase, with MF GWs second, and very little contribution from LF GWs. For PLW, ML GWs contributes most.
2. For all three probabilities, the combined increase of probabilities by two GW components, are always more than the sum of individual contributions from each individual GW component. For example, in Table 4, HF and MF GWs added to the background with LF GWs contribute to 6.0% and 5.0% increase of PDI, respectively. But when they are both present, the total PDI is increased by 15.0%.

The effects of GWs on stabilities can also be understood from the distributions shown in Figure 4, by comparing for example the black solid line (including all GWs) with the red dotted lines (>6 hr GWs). For  $N^2$ , when all waves are included, the distribution is widened and the peak is shifted toward smaller  $N^2$  values, resulting in an increase in PCI. For  $S$ , the distribution is also widened and the peak is shifted toward larger  $S$  value, resulting in increased PLW. For  $Ri$ , the distribution is narrowed (as a result of widened  $S$  distribution) with the peak shifted closer to the shaded region where  $0 < Ri < 1/4$  and significantly increases PDI.

It is interesting to compare the temperature and wind perturbation distributions in Figure 3 with the  $N^2$  and  $S$  distributions in Figure 4(a,b) for LF and HF GWs. While LF perturbations have much larger standard deviations or amplitudes, their  $N^2$  and  $S$  distributions are much narrower than HF perturbations. This is a clear indication that wave amplitude alone is not a deciding factor for creating unstable layers. The vertical scale of the perturbations is an important factor because it directly affects the lapse rate and vertical wind shear. Our results imply that for waves that can be resolved by the lidar measurements, HF GWs tend to have smaller vertical scales which result in larger vertical gradi-

PCI( %)	B (0.0%)	BH (1.3%)	BM (0.2%)	BL (0.0%)	BHM (2.7%)	BHL (1.8%)	BML (0.6%)
H	1.3	–	2.5	1.8	–	–	3.4
M	0.2	1.4	–	0.6	–	2.2	–
L	0.0	0.5	0.4	–	1.3	–	–
HM	2.7	–	–	4.0	–	–	–
HL	1.8	–	3.8	–	–	–	–
ML	0.5	2.7	–	–	–	–	–
HML	4.0	–	–	–	–	–	–

Table 2: Changes of PCI when GWs are added. The top row indicates the components in the original field with their PCIs indicated in the parentheses. The left column indicates type of GWs added. The values in the table are changes in percentage points of PCI when the GW components indicated by the left column in that row is added to the original field indicated by the top row in that column. For example, the value at the row HM and column B indicates when HF and MF GWs are added to the background, PCI is increased by 2.7 percentage points from 0.0%. See text for detailed description of all notations.

PLW( %)	B (0.2%)	BH (0.7%)	BM (0.8%)	BL (0.7%)	BHM (2.7%)	BHL(1.9%)	BML (3.3%)
H	0.5	–	1.9	1.2	–	–	3.1
M	0.6	2.0	–	2.6	–	4.5	–
L	0.5	1.2	2.5	–	3.7	–	–
HM	2.5	–	–	5.7	–	–	–
HL	1.7	–	5.6	–	–	–	–
ML	3.1	5.7	–	–	–	–	–
HML	6.2	–	–	–	–	–	–

Table 3: Same as Table 2 but for the changes of PLW.

PDI( %)	B (0.3%)	BH (3.2%)	BM (1.5%)	BL (0.9%)	BHM (8.4%)	BHL (6.9%)	BML (5.9%)
H	2.9	–	6.9	6.0	–	–	10.0
M	1.2	5.2	–	5.0	–	9.0	–
L	0.6	3.7	4.4	–	7.5	–	–
HM	8.1	–	–	15.0	–	–	–
HL	6.6	–	14.4	–	–	–	–
ML	5.6	12.7	–	–	–	–	–
HML	15.6	–	–	–	–	–	–

Table 4: Same as Table 2 but for the changes of PDI.

290 ents that LF GWs. Even though HF GWs have in general smaller amplitudes compared  
 291 with LF GWs, the increase in gradients creates both more stable and unstable regions,  
 292 thus widens the  $N^2$  and  $S$  distributions and increases all three probabilities.

#### 293 **4.2 Contributions from $N^2$ and $S$ to PDI**

294 The measure of PDI is based on  $Ri = N^2/S^2$ , which is related to both static stability  
 295  $N^2$  and vertical shear of horizontal wind  $S$ .  $0 < Ri < 1/4$  can be satisfied by small positive  
 296  $N^2$  and/or large  $S$ . In reality, when  $N^2$  positive but close to zero, convective instability is  
 297 more likely occur that dynamic instability because any small perturbations could push  $N^2$   
 298 to negative value. Uncertainty in measurements also adds to the uncertainty of whether  
 299  $N^2$  is truly positive. Therefore, if a region that satisfies  $0 < Ri < 1/4$  is only associated with  
 300 small positive  $N^2$  but not large  $S$ , it should be considered as being near convectively un-  
 301 stable, but not dynamically unstable. A more accurate estimate of the PDI should exclude  
 302 such regions.

303 To consider the contributions to a small  $Ri$  from  $N^2$  and  $S$  separately, we can rewrite  
 304 (2) as

$$\lg Ri = \lg N^2 + \lg S^2, \quad (6)$$

305 which shows that  $\lg Ri$  is sum of contributions from  $\lg N^2$  and  $\lg S^2$ . Figure 6 shows 2D  
 306 histogram of all data points with  $\lg N^2$  and  $\lg S^2$  as horizontal and vertical axes, respec-  
 307 tively. Data points with  $N^2 < 0$  are excluded in this plot. The blue diagonal line corre-

308 sponds to  $Ri=0.25$ . Area below this line is where  $0 < Ri < 0.25$  thus dynamically unsta-  
 309 ble. The cyan horizontal and vertical lines indicate medium values of  $N^2=4.2 \times 10^{-4} \text{ s}^{-2}$   
 310 and  $S=20.8 \text{ ms}^{-1} \text{ km}^{-1}$ , respectively. They separate the area below the diagonal line into  
 311 three areas, marked as A, B and C. Area A is where  $N^2$  is small and  $S$  is small; area  
 312 B is where  $N^2$  is small and  $S$  is large; area C is where  $N^2$  is large and  $S$  is large. They  
 313 make up 17%, 69%, and 14% respectively to the total data points below the diagonal line.  
 314 This shows that the majority (69%) of data points with  $0 < Ri < 0.25$  correspond to large  
 315 wind shear in a less stable stratification. A small fraction (14%) is due to even larger wind  
 316 shear in a more stable stratification. A small but not insignificant portion (17%) is due to  
 317 small  $N^2$  in the absence of large wind shear, which as described above, should not be con-  
 318 sidered as dynamically unstable. Therefore, all the PDI values we presented above slightly  
 319 overestimate the actual probably of dynamic instability due to large wind shear only. The  
 320 total PDI, if taking this into account, should be  $15.6\% \times (1-17\%) = 12.9\%$ .

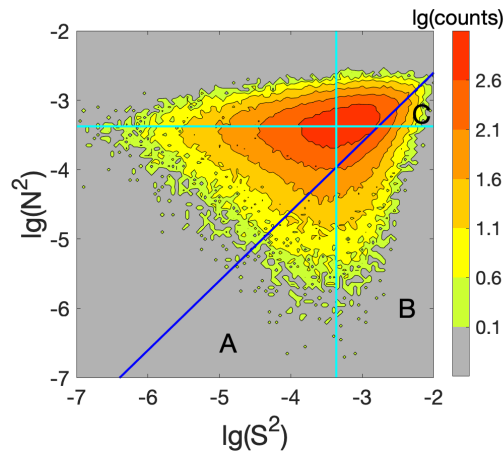


Figure 6: 2D histogram of all data points as a function of both  $\ln S^2$  and  $\ln N^2$ . The blue diagonal line represents where  $Ri=0.25$ . The cyan horizontal and vertical lines indicate medium values of  $N^2=4.2 \times 10^{-4} \text{ s}^{-2}$  and  $S=20.8 \text{ ms}^{-1} \text{ km}^{-1}$ , respectively. The color shades are linear in  $\lg(\text{counts})$  as indicated by the color bar. The bin sides are both 0.05 for horizontal and vertical axis.

## 321 5 Conclusion

322 In this paper, we presented analyses of the probabilities of convective and dynamic  
 323 instabilities and large wind shear (PCI, PDI, PLW) in the mesopause region over the An-  
 324 des using 2170 hours of high resolution temperature and wind measurements from a Na

325 lidar at ALO. The data was acquired over 5 years in 244 nights and covers all calendar  
326 months. These three probabilities corresponds to  $N^2 < 0$ ,  $S > 40 \text{ ms}^{-1}$ , and  $0 < Ri < 0.25$ , re-  
327 spectively. Biases in these probabilities due to measurement errors were carefully analyzed  
328 and eliminated. The overall PCI, PDI and PLW from all the lidar data are 4.0%, 6.2%,  
329 and 15.6%, respectively. Therefore, dynamic instability is much more likely to occur than  
330 convective instability. This is similar to the results at Fort Collins (41°N, 105°W), where  
331 *Sherman and She* [2006] obtained a PCI of less than 1.4% and a PDI ranging from 2.7%  
332 to 6.0%, and at Sao Jose dos Campo (23.1°S, 45.5°W) where *Andrioli et al.* [2017] ob-  
333 tained PCI of 3% and PDI of 17.5%, although these analyses were made with data at  
334 coarser resolutions.

335 The impacts of GWs on these probabilities were analyzed by separating the data  
336 in to HF, MF and LF and background, and separately calculating the probabilities. We  
337 found that HF GWs contribute most to the increase of PCI and PDI and LF GWs con-  
338 tribute the least. Our analyses also show that the total increase of probabilities by two GW  
339 components is always more than the sum of increases from each GW component. For ex-  
340 ample, HF and MF GWs added to the background with LF GWs contribute to 6.0% and  
341 5.0% increase of PDI, respectively. But when they are both present, the total PDI is in-  
342 creased by 15.0%. *Yue et al.* [2010] reported tides can contribute significantly to the large  
343 wind shears in the MLT. *Zhao et al.* [2003] reported that tides alone are usually not strong  
344 enough to induce instability, but they can establish the environment for instabilities to de-  
345 velop. These results are consistent with our findings and support the notion that simulta-  
346 neous presence of waves at multiple time scales can significantly increase the probabilities  
347 of instabilities.

348 We also found that while LF GWs have much larger overall amplitudes than HF  
349 GWs, they contribute less to the perturbations in  $N^2$  and  $S$  than HF GWs. This indicates  
350 that it is the small vertical scale of HF GWs that largely contribute to their ability of cre-  
351 ating unstable layers. Although LF GWs have large amplitude, their larger vertical scale  
352 does not create as large vertical gradients in temperature and horizontal wind needed for  
353 instability that HF GWs do.

## 354 **A Bias correction for probabilities**

355 Bias of probabilities of instabilities are primarily due to temperature and wind mea-  
 356 surement errors. Bias can be estimated by analytical method and numerical method. An-  
 357 alytical bias correction of PCI has been presented by *Zhao et al.* [2003]. In their work,  
 358 PCI is expressed as a function of the uncertainties of  $N^2$ . The uncertainties of  $N^2$  are ap-  
 359 proximately expressed as a function of the uncertainties of  $T$  errors. However, an analyt-  
 360 ical formula for bias of PDI is much more complicated and requires more approximation  
 361 than the formula for bias of PCI since  $Ri$  is related to both temperature and wind mea-  
 362 surements. More approximation may lead to extra bias from the bias correction formula  
 363 itself. Numerical method can avoid this issue. A numerical method Monte-Carlo simula-  
 364 tion is applied to numerically calculate the bias of PCI, PLW and PDI.

365 Detailed process for Monte-Carlo simulation is as follow. A series of artificial er-  
 366 rors are added to temperature and wind measurements. The added errors to  $U$  and  $V$  are  
 367 Gaussian distributed with uncertainties from 0 to 15  $\text{ms}^{-1}$ . From the measurement, the un-  
 368 certainties of  $U$  and  $V$  error at the same time and the same altitude are found to be almost  
 369 the same. The added errors to  $T$  are Gaussian distributed with uncertainties from 0 to 8 K.  
 370 The uncertainties of artificial errors cover all the possible uncertainties of ALO lidar mea-  
 371 surement errors. In our simulations, multiple combinations of errors of temperature and  
 372 horizontal winds with different distribution uncertainties are added. From simulation re-  
 373 sults, the bias of PDI contributed from errors of  $T$  is found to be neglectable. So bias  
 374 of PDI is treated as a function of uncertainties of  $U/V$  error distribution. Biases of PCI,  
 375 PLW and PDI calculated through Monte-Carlo simulations are presented in Figure 7. For  
 376 PCI, as the uncertainty of  $T$  error increases, as do the bias, shown as the red solid line.  
 377 The bias of PLW rises with uncertainty of  $U/V$  error, shown as the black dashed line. For  
 378 PDI, shown as the blue line with star markers, the bias decreases and then increases with  
 379 uncertainty of  $U/V$  error. The bias line is with a valley value around  $-5\%$  when the un-  
 380 certainty of  $U/V$  error is about 7  $\text{ms}^{-1}$ .

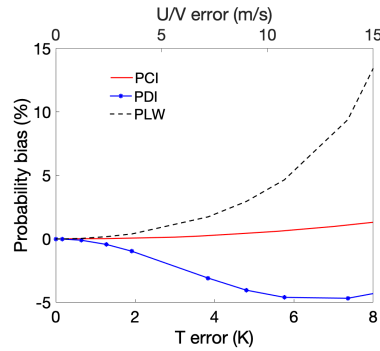


Figure 7: Biases of PCI, PLW and PDI with respect to measurement errors with different Gaussian distribution uncertainties. PCI (red solid line) is a function of uncertainties of temperature error distribution. PDI (black dashed line) and PLW (blue solid line with star markers) are functions of uncertainties of horizontal wind error distribution.

## 6 Open Research

The routine ALO Na Lidar data [*ALOLidar* [2014-present]] between 80-105 km and contour plots are available at <http://alo.erau.edu/data/nalidar/>. The software used for analysis and plotting is MATLAB\_R2018a [*MATLAB* [2018]].

## Acknowledgments

This work and the Na lidar operation at ALO is being supported by the National Science Foundation (NSF) grants AGS-1759471.

## References

- Achatz, U. (2007), Gravity-wave breaking: Linear and primary nonlinear dynamics, *Adv. Space Res.*, 40(6), 719–733, doi:10.1016/j.asr.2007.03.078.
- ALOLidar (2014-present), Andes lidar observatory.
- Andreassen, Ø., C. E. Wasberg, D. C. Fritts, and J. R. Isler (1994), Gravity wave breaking in two and three dimensions: 1. model description and comparison of two-dimensional evolutions, *J. Geophys. Res. Atmos.*, 99(D4), 8095–8108, doi:10.1029/93JD03435.
- Andreassen, Ø., P. Ø. Hvidsten, D. C. Fritts, and S. Arendt (1998), Vorticity dynamics in a breaking internal gravity wave. part 1. initial instability evolution, *J. Fluid Mech.*, 367,

- 397 27–46, doi:10.1017/S0022112098001645.
- 398 Andrioli, V. F., P. P. Batista, J. Xu, G. Yang, W. Chi, and L. Zhengkuan (2017),  
 399 Strong temperature gradients and vertical wind shear on mlt region associated to  
 400 instability source at 23s, *J. Geophys. Res. Space Physics*, *122*(4), 4500–4511, doi:  
 401 10.1002/2016JA023638.
- 402 Cao, B., and A. Z. Liu (2016), Intermittency of Gravity Wave Momentum Flux in the  
 403 Mesopause Region Observed with an All-Sky Airglow Imager, *J. Geophys. Res. Atmos.*,  
 404 *121*, doi:10.1002/2015JD023,802, doi:10.1002/2015JD023802.
- 405 Dong, B., and K. C. Yeh (1988), Resonant and nonresonant wave-wave interactions  
 406 in an isothermal atmosphere, *J. Geophys. Res. Atmos.*, *93*(D4), 3729–3744, doi:  
 407 10.1029/JD093iD04p03729.
- 408 Fritts, D. C., and P. K. Rastogi (1985), Convective and dynamical instabilities due to grav-  
 409 ity wave motions in the lower and middle atmosphere: Theory and observations, *Radio*  
 410 *Sci.*, *20*(6), 1247–1277, doi:10.1029/RS020i006p01247.
- 411 Fritts, D. C., and L. Yuan (1989), Stability analysis of inertia-gravity wave structure  
 412 in the middle atmosphere, *J. Atmos. Sci.*, *46*(12), 1738–1745, doi:10.1175/1520-  
 413 0469(1989)046<1738:SAOIWS>2.0.CO;2.
- 414 Gardner, C. S., and W. Yang (1998), Measurements of the dynamical cooling rate associ-  
 415 ated with the vertical transport of heat by dissipating gravity waves in the mesopause  
 416 region at the Starfire Optical Range, New Mexico, *J. Geophys. Res.*, *103*(D14), 16,909–  
 417 16,926, doi:10.1029/98JD00683.
- 418 Gardner, C. S., Y. Zhao, and A. Z. Liu (2002), Atmospheric stability and gravity wave  
 419 dissipation in the mesopause region, *J. Atmos. Sol.-Terr. Phys.*, *64*(8), 923 – 929, doi:  
 420 [https://doi.org/10.1016/S1364-6826\(02\)00047-0](https://doi.org/10.1016/S1364-6826(02)00047-0).
- 421 Hecht, J. H., D. C. Fritts, L. J. Gelinas, R. J. Rudy, R. L. Walterscheid, and A. Z. Liu  
 422 (2021), Kelvin-Helmholtz billow interactions and instabilities in the mesosphere  
 423 over the Andes Lidar Observatory: 1. Observations, *J. Geophys. Res. Atmos.*, *126*(1),  
 424 e2020JD033,414, doi:10.1029/2020JD033414.
- 425 Hines, C. O. (1971), Generalizations of the richardson criterion for the on-  
 426 set of atmospheric turbulence, *Q.J.R. Meteorol. Soc.*, *97*(414), 429–439, doi:  
 427 10.1002/qj.49709741405.
- 428 Hodges, R. R., Jr (1967), Generation of turbulence in the upper atmosphere by internal  
 429 gravity waves, *J. Geophys. Res.*, *72*(13), 3455–3458, doi:10.1029/JZ072i013p03455.

- 430 Klostermeyer, J. (1991), Two- and three-dimensional parametric instabilities in finite-  
431 amplitude internal gravity waves, *Geophys. Astrophys. Fluid Dyn.*, *61*, 1–25.
- 432 Larsen, M. F. (2002), Winds and shears in the mesosphere and lower thermosphere: Re-  
433 sults from four decades of chemical release wind measurements, *J. Geophys. Res. Space*  
434 *Physics*, *107*(A8), SIA 28–1, doi:10.1029/2001JA000218.
- 435 Li, F., A. Z. Liu, G. R. Swenson, J. H. Hecht, and W. A. Robinson (2005a), Observations  
436 of gravity wave breakdown into ripples associated with dynamical instabilities, *J. Geo-*  
437 *phys. Res.*, *110*(D9), doi:10.1029/2004JD004849.
- 438 Li, F., A. Z. Liu, and G. R. Swenson (2005b), Characteristics of instabilities  
439 in the mesopause region over Maui, Hawaii, *J. Geophys. Res.*, *110*(D9), doi:  
440 10.1029/2004JD005097.
- 441 Liu, A. Z., Y. Guo, F. Vargas, and G. R. Swenson (2016), First measurement of horizon-  
442 tal wind and temperature in the lower thermosphere (105–140 km) with a Na Lidar at  
443 Andes Lidar Observatory, *Geophys. Res. Lett.*, *43*, doi:10.1002/2016GL068461.
- 444 Liu, H.-L. (2017), Large wind shears and their implications for diffusion in regions with  
445 enhanced static stability: The mesopause and the tropopause, *J. Geophys. Res. Atmos.*,  
446 *122*(18), 9579–9590, doi:10.1002/2017JD026748.
- 447 Liu, H.-L., P. B. Hays, and R. G. Roble (1999), A numerical study of gravity wave break-  
448 ing and impacts on turbulence and mean state, *J. Atmos. Sci.*, *56*(13), 2152–2177, doi:  
449 10.1175/1520-0469(1999)056<2152:ANSOGW>2.0.CO;2.
- 450 Liu, X., J. Xu, H.-L. Liu, J. Yue, and W. Yuan (2014), Simulations of large winds and  
451 wind shears induced by gravity wave breaking in the mesosphere and lower thermo-  
452 sphere (MLT) region, *Ann. Geophys.*, *32*(5), 543–552, doi:10.5194/angeo-32-543-2014.
- 453 Lombard, P. N., and J. J. Riley (1996), Instability and breakdown of internal grav-  
454 ity waves. i. linear stability analysis, *Physics of Fluids*, *8*(12), 3271–3287, doi:  
455 10.1063/1.869117.
- 456 MATLAB (2018), Matlab\_r2018a.
- 457 Miles, J. W. (1961), On the stability of heterogeneous shear flows, *J. Fluid Mech.*, *10*(4),  
458 496 – 508, doi:10.1017/S0022112061000305.
- 459 Phillips, O. M. (1977), *The dynamics of the upper ocean*, 2d ed., 336 pp., Cambridge Uni-  
460 versity Press Cambridge.
- 461 She, C.-Y., A. Z. Liu, T. Yuan, J. Yue, T. Li, C. Ban, and J. Friedman (2021), MLT Sci-  
462 ence Enabled by Atmospheric Lidars, in *Upper Atmosphere Dynamics and Energetics*,

- 463 edited by W. Wang, Y. Zhang, and L. Paxton, pp. 395–450.
- 464 Sherman, J. P., and C.-Y. She (2006), Seasonal variation of mesopause region wind shears,  
465 convective and dynamic instabilities above Fort Collins, CO: A statistical study, *J. At-*  
466 *mos. Sol.-Terr. Phys.*, *68*(10), 1061 – 1074, doi:10.1016/j.jastp.2006.01.011.
- 467 Sonmor, L. J., and G. P. Klaassen (1997), Toward a unified theory of grav-  
468 ity wave stability, *J. Atmos. Sci.*, *54*(22), 2655–2680, doi:10.1175/1520-  
469 0469(1997)054<2655:TAUTOG>2.0.CO;2.
- 470 Yue, J., C.-Y. She, and H.-L. Liu (2010), Large wind shears and stabilities in the  
471 mesopause region observed by Na wind-temperature lidar at midlatitude, *J. Geophys.*  
472 *Res. Space*, *115*(A10), doi:10.1029/2009JA014864.
- 473 Zhao, Y., A. Z. Liu, and C. S. Gardner (2003), Measurements of atmospheric stability in  
474 the mesopause region at starfire optical range, NM, *J. Atmos. Sol.-Terr. Phys.*, *65*(2), 219  
475 – 232, doi:10.1016/S1364-6826(02)00288-2.